ACS Catalysis

Research Article

Cite This: ACS Catal. 2020, 10, 562−569

pubs.acs.org/acscatalysis

Atomically Embedded Ag via Electrodiffusion Boosts Oxygen Evolution of CoOOH Nanosheet Arrays

Changsoo Lee,[†] Kihyun Shin,[‡] Chanwon Jung,[†] Pyuck-Pa Choi,[†] Graeme Henkelman,*[,‡] and Hyuck Mo Lee*[,†]

[†]Department of Materials Science and Engineering, KAIST, 291 Daehak-ro, Yuseong-gu, Daejeon 34141, Republic of Korea

[‡]Department of Chemistry, and the Oden Institute for Computational Engineering and Sciences, University of Texas at Austin, Austin, Texas 78712, United States

Supporting Information

ABSTRACT: Layered cobalt (oxy)hydroxides have received much attention as cost-effective and efficient catalysts for the oxygen evolution reaction (OER) for electrochemical water splitting. Doping with guest cations possessing different oxidation states such as Ag can change the chemistry of conventional transition metal oxides and hydroxides, generating unexpected electrocatalytic performances. However, Ag dopants have been found to easily segregate at the surface of electrocatalysts, which induces deactivation. Here, we fabricated Ag-doped CoOOH nanosheet arrays using electrochemical deposition, followed by a simple electrochemical diffusion approach. Surprisingly, we revealed, through atom probe tomography (APT), secondary ion mass spectroscopy (SIMS), and energy-dispersive spectroscopy (EDS) that Ag atoms are homogeneously distributed without any detectable segregation. The Ag-doped CoOOH exhibits enhanced OER performance in terms of overpotential, both experimentally (256 mV) and theoretically (60 mV). The homogeneously distributed Ag dopants facilitate the phase transformation from $Co(OH)_2$ to the active phase of CoOOH. Calculations show that Ag doping enhances phase stability of CoOOH and exposed Ag dopants act as active sites by releasing −OH adsorbates.

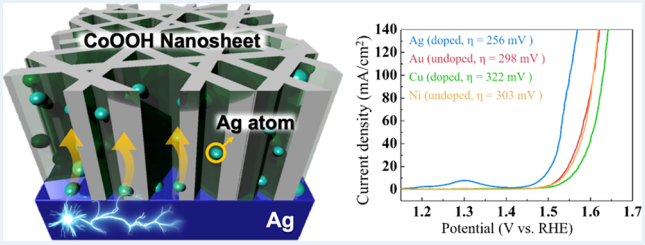

KEYWORDS: *oxygen evolution reaction, cobalt oxyhydroxide, electrochemical diffusion, layered structure, density functional theory*

1. INTRODUCTION

Renewable energy technologies are required to mitigate global climate change and the depletion of natural energy sources. Among the many approaches, water electrolysis has received great attention as a promising technology for renewable and clean energy sources.[1,2] The oxygen evolution reaction (OER), showing much more sluggish kinetics than the hydrogen evolution reaction (HER), governs the overall activity of water electrolysis.[3,4] Precious metal oxides such as IrO_2 and RuO_2 are considered to be state-of-the-art electrocatalysts, possessing exceptional OER activities over a wide range of pH values.[5] However, suffering from high cost and poor stability, precious metal oxides have not been commercialized yet. Thus, developing earth-abundant, highly active, and durable electrocatalysts is considered an urgent issue for water electrolysis.

Transition metal oxides, (oxy)hydroxides, and chalcogenides have been widely studied.[6−8] Among them, the Co-based oxides and (oxy)hydroxides have been proven to possess acceptable costs, desirable activity, and stability in alkaline media.[9−13] Favaro et al. investigated the active phase of Co-based oxides and hydroxides in terms of oxidation states of Co using operando ambient-pressure X-ray photoelectron spectroscopy (XPS) measurements under applied potentials.[14] Both the Co_3O_4 (Co^{2+} and Co^{3+}) and $Co(OH)_2$ (Co^{2+}) phases showed phase transformations into CoOOH (Co^{3+}) in alkaline media, along with further oxidations to the Co^{4+} state.[15] These higher oxidation states of Co are known to be robust active sites for water oxidation,[16] which encouraged us to design OER catalysts with these active sites.

One effective way to generate higher oxidation states is by doping with other metal ions.[13,17] Zhao et al. reported Ag-doped $CoSe_2$ electrocatalysts via a simple cation exchange method and demonstrated a significant improvement in the OER activity.[18] They reported that only 1% of Ag doping could enhance the electrical conductivity of $CoSe_2$, thereby making Co^{2+} more easily transformed to higher oxidation states such as Co^{3+} and Co^{4+}. Likewise, there have been many attempts to introduce Ag dopants in oxide and hydroxide systems.[19,20] However, Ag atoms tend to segregate to the surface of electrocatalysts with conventional doping methods such as cation exchange[19] and codeposition.[21] The formed Ag_2O phase possesses very poor activity with respect to the OER.[22] Thereby, surface segregation of Ag atoms causes the deactivation of the catalysts.

Received: May 30, 2019
Revised: November 5, 2019
Published: December 3, 2019

DOI: 10.1021/acscatal.9b02249
ACS Catal. 2020, 10, 562−569

Herein, we developed a simple electrochemical activation method to form highly uniform and reproducible Ag-doped CoOOH nanosheet arrays, which was motivated by the diffusion phenomenon between metallic substrates and insulating layers in resistive switching memory devices.[23,24] We applied this method to electrodeposited $Co(OH)_2$, inducing an electrochemical diffusion of Ag atoms from the metallic substrate and a simultaneous phase transformation of $Co(OH)_2$ to CoOOH. We confirmed homogeneously distributed Ag dopants, without any detectable segregation, using various analytical methods such as atom probe tomography (APT), secondary ion mass spectroscopy (SIMS), and energy-dispersive X-ray spectroscopy (EDS). Based on the experimental results and density functional theory (DFT) calculations, we discuss the improvements in the OER catalytic properties of Ag-doped CoOOH, comparing with undoped CoOOH for Au or Ni substrates.

2. METHODS

2.1. Materials. Cobalt nitrate hexahydrate ($Co(NO_3)_2 \cdot 6H_2O$, >98.0%), sodium nitrate ($NaNO_3$, >99.9%), and potassium hydroxide (KOH, >99.99%) were all purchased from Sigma-Aldrich. Polycrystalline gold, silver, copper, and nickel thin films (thickness = 0.05 mm, purity = 99.95, 99.98, 99.9, and 99.9%, respectively) were purchased from Nilaco Corporation. Milli-Q ultrapure water (>18 MΩ·cm) was used in all experiments.

2.2. Preparation of Electrocatalysts. All metal substrates were polished with sandpaper (#2000) and washed three times with ultrapure water to obtain clean surfaces for electrodeposition. The geometrical surface area was about 0.75 cm^2. $Co(OH)_2$ thin films were fabricated using a two-step electrodeposition process. As a first step, a constant current of 1 mA/cm^2 was applied for 100 s on the metal substrates. For further growth of $Co(OH)_2$, a higher constant current of 10 mA/cm^2 was applied for 60 s. Cobalt nitrate (1.0 M) and sodium nitrate (1.0 M) dissolved in deionized water (>18 MΩ·cm) were used as the cobalt precursor and the supporting electrolyte, respectively. After electrodeposition, a constant voltage of 1.4 V (vs RHE) was applied in an O_2-saturated 1.0 M KOH electrolyte to induce phase transformation of $Co(OH)_2$ to CoOOH and electrochemical diffusion.

2.3. Electrochemical Measurements. Electrocatalysts in a conventional three-electrode configuration were tested with a potentiostat (Interface 1010E, Gamry Instrument). Hg/HgO (filled with 20 wt % KOH) and a Pt wire were used as the reference and counter electrodes, respectively. All electrochemical measurements were conducted in alkaline media of O_2-saturated 1.0 M KOH (pH 14). The applied potentials in this work were referenced to a revisable hydrogen electrode (RHE) through standard calibration.[25] The OER was evaluated by performing linear sweep voltammetry (LSV) in a voltage range from 1.0 to 1.8 V (vs RHE) at a scan rate of 5 mV/s. All electrochemical measurements were iR-corrected using the CI method implemented in the Gamry software. To evaluate the charge transfer resistance, electrochemical impedance spectroscopy (EIS) measurements were carried out by applying an AC voltage of 10 mV in the frequency range of 100−0.1 kHz at 1.53 V (vs RHE). A chronopotentiometry experiment with 10 mA/cm^2 was carried out for durability testing, and LSV was conducted before and after the durability test.

2.4. Material Characterization. Surface morphology, microstructures, elemental distributions, and compositions were analyzed using field-emission scanning electron microscopy (FE-SEM) (Nova230, FEI), transmission electron microscopy (TEM) (Talos F200X, FEI operated at 200 kV), energy-dispersive X-ray spectroscopy (EDS), and inductively coupled plasma optical emission spectroscopy (ICP-OES) (Ailent ICP-OES 5110, Agilent), respectively. For cross-sectional EDS mapping, TEM samples were prepared by focused ion beam (FIB) milling (Hellios G4, FEI). To prepare the APT tips, a 500 nm layer of Cr was deposited on the surface of the electrochemically activated Ag-doped CoOOH by using an electron beam evaporator (KVET-C500200, Korea Vacuum). Subsequently, the backside lift-out specimen preparation method[26] was applied to prevent microfractures in the porous catalyst layer, as shown in Figure S1. The electrocatalysts were structurally characterized using a thin-film X-ray diffractometer (XRD, Ultima IV, Rigaku) with 2θ measurements (with 2° graze angle) to reduce detection of substrate peaks. The micrometer-scale elemental distribution was investigated by time-of-flight secondary ion mass spectrometry (TOF-SIMS) (Ion-TOF GmbH). In addition, atom probe tomography (APT) (LEAP4000X HR, CAMECA) measurements were performed using a local electrode atom probe in pulsed laser mode at 40 K. The laser pulse energy and frequency were 80 pJ and 125 kHz, respectively. The existence of the CoOOH phase was verified using X-ray photoelectron spectroscopy (XPS) (K-α, Thermo VG Scientific) with Al Kα radiation (1486.6 eV). All energy data were calibrated with a carbon 1s binding energy (284.8 eV) for C−C components.

2.5. Computational Details. Generalized gradient approximation (GGA)-level spin-polarized density functional theory (DFT) calculations were performed with the Vienna ab initio simulation package using a plane wave basis set with a cut-off energy of 400 eV. The Perdew−Burke−Ernzerhof functional[27] was used to describe electron exchange and correlation. The DFT + U method was employed to treat localized Co 3d orbitals with an effective U value of 3.52 eV, as reported in our previous research[28] and in other studies.[29] The Brillouin zone was sampled with a 2 × 2 × 1 k-point mesh following the Monkhorst−Pack scheme. The convergence criteria for electronic and geometrical optimization were 10^{-5} eV and 0.01 eV/Å, respectively. We constructed a CoOOH slab model for the $(10\bar{1}4)$ surface, which is known as the most active surface for the OER.[28] We investigated three different surfaces of CoOOH, (0001), $(01\bar{1}2)$, and $(10\bar{1}4)$, and found that $(10\bar{1}4)$ has the highest stability and lowest overpotential among surfaces under the OER operating condition. We considered Ag doping by substituting a Co atom in the first layer. The slab was constructed by expanding to a 2 × 2 supercell, which was approximately 7 Å thick, with the bottom half of the layers fixed in their bulk positions. A surface Pourbaix diagram[30] was calculated to identify the stable surface configuration. This is important because water molecules are easily dissociated on metal oxide substrates under OER conditions.[31,32] Specifically, surface structures with water and various adsorbates were considered to determine a realistic surface model to study reaction mechanisms. The OER overpotential was found by a reaction energy diagram, which is drawn using the following equation[33]

$$\Delta G(U) = \Delta E - \Delta E_{ZPE} - T\Delta S - neU$$

DOI: 10.1021/acscatal.9b02249
ACS Catal. 2020, 10, 562−569

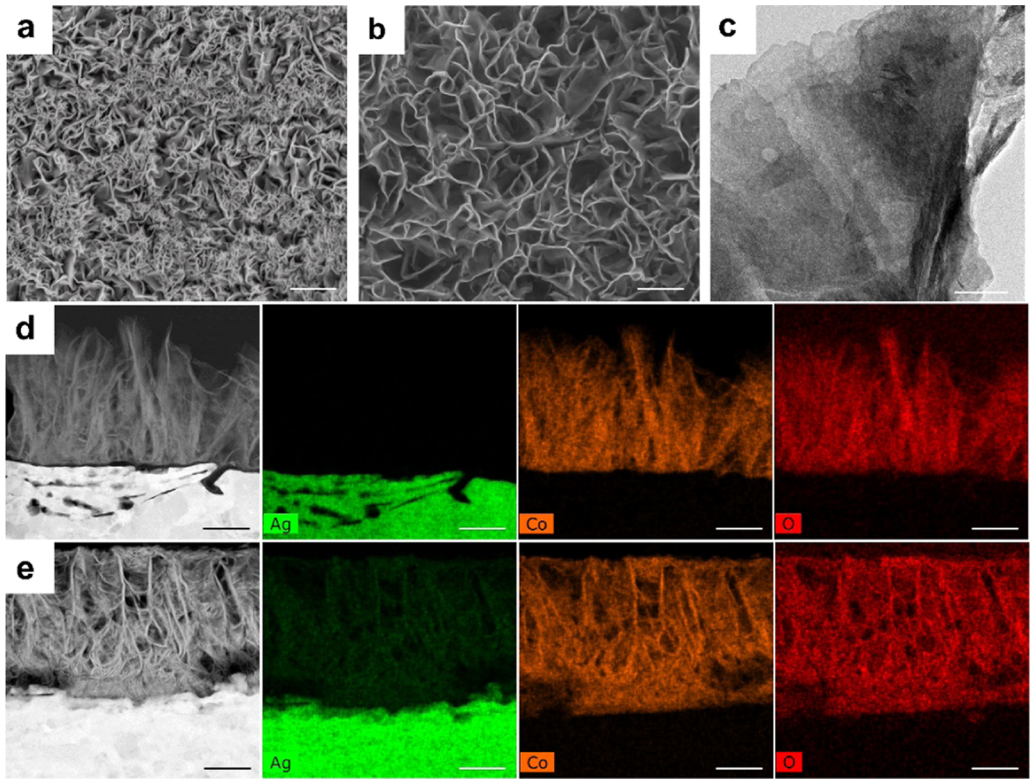

Figure 1. Ag-doped CoOOH nanosheet arrays. (a, b) SEM images of the surface morphology of Ag-doped CoOOH nanosheet arrays; (c) TEM image of exfoliated Ag-doped CoOOH; and (d, e) EDS elemental mapping of a cross-section of Ag-doped CoOOH prepared by FIB before and after the activation process, respectively. Scale bars: (a) 1 μm; (b) 500 nm; (c) 100 nm; and (d, e) 200 nm.

where ΔE is the reaction energy, ΔZPE represents the zero-point energy correction, ΔS is the difference in entropy, and U is the applied potential.

3. RESULTS AND DISCUSSION

3.1. Electrodiffused Ag Atoms in CoOOH Nanosheet Arrays. To compare the effect of doping for various metallic elements, $Co(OH)_2$ electrocatalysts with layered structures were electrochemically deposited on Ag, Au, Cu, and Ni thin films using the two-step electrodeposition, followed by electrochemical activation at 1.4 V for 100 s. In the electrodeposition step, the Co^{2+} ions in the solution are combined with OH^- species from the reduction of NO^{3-} anions and transformed into a $Co(OH)_2$ phase.[34,35] $Co(OH)_2$ can be further oxidized to a CoOOH phase, containing Co^{3+} with a higher oxidation state, by the activation process.[36,37] As shown in Figure 1a–c, the CoOOH fabricated on Ag has a dense layered structure. No notable morphology difference with CoOOH on other substrates, such as Au, Cu, and Ni, was detected in the SEM images in Figure S2a–d. Cross-sectional EDS maps of CoOOH on Ag substrates were obtained before and after activation to confirm the elemental diffusion via the activation process. Figure 1d,e clearly reveals that Ag atoms have diffused into the CoOOH layers from the substrate after the activation process. Furthermore, from the measured EDS maps and compositions of nanosheets, prepared by exfoliating with ultrasonication (see Figure S3a and Table S1), Cu also diffused from the substrate into CoOOH nanosheets, whereas, the diffusion of Au and Ni was not detected. As shown in the lattice fringes in the high-resolution transmission electron microscopy (HRTEM) image (Figure S4a), a lattice spacing of approximately 0.247 and 0.143 nm were observed, assigned to the $(10\bar{1}0)$ and $(11\bar{2}0)$ planes of the CoOOH phase, respectively. Moreover, the fast-Fourier transformed selected area diffraction pattern (FFT-SAED) (Figure S4b) indicates that the Ag-doped CoOOH nanosheet arrays have a polycrystalline structure with the CoOOH phase. An XPS analysis of the Ag 3d core level shows that the oxidation state of the dispersed Ag atoms is +1, implying ionic diffusion of Ag (see Figure S5a). The electrochemical diffusion of Ag is initiated at 1.15 V and saturated over 1.35 V prior to the OER, which cannot affect the faradaic current density of OER, as shown in the quantitative XPS data in Figure S5b. To check the saturation of Ag doping via the electrochemical diffusion process, we measured Ag/Co atomic ratio of the exfoliated Ag-doped CoOOH electrocatalysts along with activation time using EDS and ICP-OES measurements (shown in Figure S6). The ratio of Ag/Co gradually increased and was saturated from 100 s. Even after applying constant voltage for 10 h at an overpotential of 300 mV, the saturated ratio of Ag/Co rarely changed. Additionally, it was confirmed that the electrochemical diffusion approach used in this work can be extended to different dopants, such as Cu, Zn, and Sn, thereby enabling a novel widely applicable approach for the design of electrocatalysts (see Figure S3a–c).

3.2. Characterization of Atomically Embedded Ag Atoms. Homogeneous distribution of Ag dopants without segregation through the facile electrochemical method is one of our key results. Thus, we conducted various chemical analyses from the atomic scale to microscale. First, a random distribution of Ag dopants without any indications of segregation was confirmed with high-angle annular dark-field scanning transmission electron microscopy (HAADF-STEM) image (see Figure 2a). As shown in Figure 2b, the atomically

DOI: 10.1021/acscatal.9b02249
ACS Catal. 2020, 10, 562–569

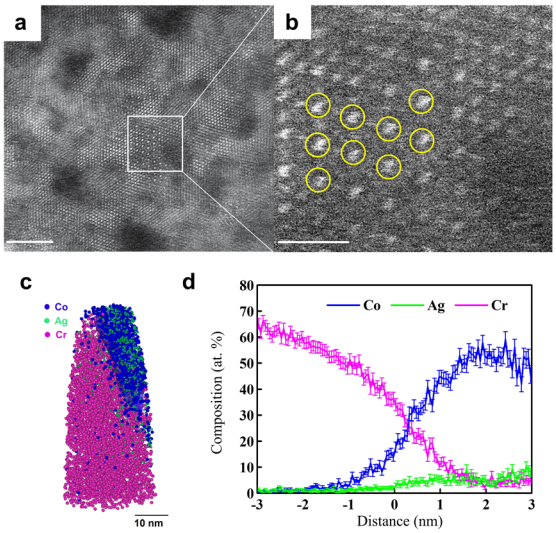

Figure 2. Atomically embedded Ag dopants. (a, b) High-resolution HAADF-STEM images for CoOOH on Ag after activation process; yellow circles indicate atomic-resolved Ag atoms, APT data obtained after the activation: (c) 3D atom maps of the Ag-doped CoOOH including the isoconcentration surface of 20 atom % Co; and (d) proximity histograms across Ag-doped CoOOH and deposited Cr interface. Scale bars: (a) 4 nm; (b) 1 nm.

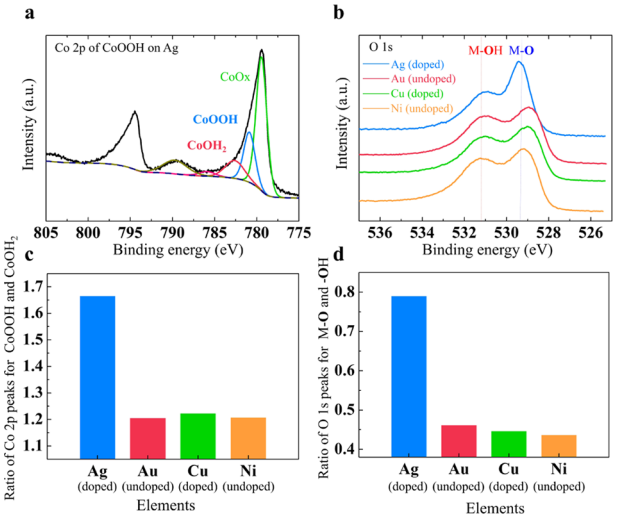

Figure 3. Ag doping effects on CoOOH phase stability in terms of oxidation state. (a) XPS Co 2p peak of CoOOH on Ag; (b) XPS O 1s peaks of CoOOH on Ag, Au, Cu, and Ni; and (c, d) quantitative analyses of deconvoluted Co 2p peaks and O 1s peaks, respectively.

resolved HADDF-STEM image shows the embedded Ag atoms substituting for Co cation sites (see the yellow circle; the brighter atoms indicate Ag dopants). Furthermore, APT measurement was carried out to investigate the distribution of Ag dopants at the sub-nanometer scale. The three-dimensional (3D) atom maps of Co, Ag, and Cr and the proxigram drawn using an isoconcentration surface of 20 atom % of Co for Ag-doped CoOOH reveal the absence of surface segregation and homogeneously distributed Ag dopants near the surface (see Figure 2c,d). At the micrometer scale, the Ag atoms are distributed homogenously in CoOOH without any detectable segregation, as shown in the SIMS 3D rendering and depth profiles in Figure S7a–c. To confirm an amount of the diffused Ag dopants in the electrocatalytic layer, we measure the composition of the exfoliated Ag-doped CoOOH electrocatalysts using ICP-OES. The measured composition is Co/Ag = 57.8:42.2 atom %, comparable to EDS composition (Co/Ag = 60.5:39.5 atom %) shown in Table S1. Additionally, the Ag-doped CoOOH was heat-treated to force segregations at the surface of electrocatalysts. As a result, the heat-treated Ag-doped CoOOH shows noticeable segregations at the surface of the electrocatalysts, as shown in the HADDF-STEM images (see Figure S8a,b).

3.3. Enhanced Phase Stability of Ag-Doped CoOOH.

To reveal the effect of Ag doping on the phase stability of CoOOH and $Co(OH)_2$ in terms of oxidation states, we performed a detailed XPS analysis of the Co 2p and O 1s peaks (shown in Figure 3a,b). The Co $2p_{3/2}$ signal can be divided into three peaks through deconvolution with respect to the Co phases.[38] The main peak at approximately 779 eV is observed in all of the Co oxide and hydroxide phases, such as $Co(OH)_2$, Co_3O_4, and CoOOH. Peaks at approximately 781.7 and 782.5 eV are assigned to CoOOH and $Co(OH)_2$, respectively. Peaks with higher binding energy at approximately 785.5 and 790.0 eV correspond to satellite peaks for $Co(OH)_2$ and CoOOH, respectively. Before the activation process, dominant $Co(OH)_2$ peaks were observed, while the ones for CoOOH were negligible (see Figure S9a). On the other hand, the peaks for CoOOH increased considerably, after the activation process. These results indicate that the electrodeposited $Co(OH)_2$ were successfully phase-transformed to the CoOOH phase with higher oxidation state via the electrochemical activation process. The Co 2p XPS peaks acquired for other substrates, after the activation process, are shown in Figure S10. The deconvoluted Co 2p peaks were analyzed using the sensitivity factors of each element and the background corrected area.[39] The relative ratios of CoOOH and $Co(OH)_2$ for the electrocatalysts are plotted in Figure 3c. It can be clearly seen that CoOOH with Ag contains a higher content of the CoOOH phase, which is ascribed to the dispersed Ag atoms. The XPS O 1s feature possesses two peaks through deconvolution corresponding to metal–O (M–O, 529.9 eV) and metal–OH (M–OH, 531.0 eV).[38,40,41] Figure S9b shows the O 1s peaks of Ag-doped CoOOH before and after the activation process. Like Co 2p XPS analysis, the O 1s peak for M–O, which was not to be observed before the activation, increased considerably after the activation. The peak intensity of M–O in the Ag substrate is distinctly higher than those of M–O in the other substrates (see Figure 3b), indicating that the electrocatalysts on the Ag substrate comprise numerous Co–O or Ag–O bonds. Similar to the Co 2p case, we calculated the ratio of the two O 1s deconvoluted peaks (see Figure 3d) and found that the electrocatalysts containing Ag have much higher M–O peaks than the electrocatalysts on other substrates. As mentioned above, the as-deposited $Co(OH)_2$ phase is transformed into the CoOOH phase, which is a well-known active phase, in the OER environment. The transformed CoOOH phase naturally goes back to the thermodynamically favored initial state ($Co(OH)_2$), after stopping the applied potential.[15,37] It is confirmed from the XPS analysis that the electrocatalyst on the Ag substrate contains an abundant remaining amount of the CoOOH phase after the OER. Also, XRD analysis supports that the homogeneously distributed Ag atoms stabilize the CoOOH phase, as shown in Figure S11. The XRD peaks at approximately 9 and 33° stemming from the $Co(OH)_2$ phase vanish in the case of the Ag substrate, while the peaks at

DOI: 10.1021/acscatal.9b02249
ACS Catal. 2020, 10, 562–569

approximately 21° corresponding to the CoOOH phase increase. The stabilization of the CoOOH phase occurs (see XRD in Figure S12) after the activation process with Ag diffusion.

3.4. Evaluation of Electrocatalytic Oxygen Evolution Performance. The electrochemical activities of the CoOOH on metal substrates toward the OER were investigated by recording linear sweep voltammetry (LSV) over a voltage range of 1.0−1.8 V in O_2-saturated 1.0 M KOH. Typically, the applied voltage, showing 10 mA/cm^2 of geometrical current density, −1.23 V is considered the overpotential for the OER.[42] As shown in Figure 4a, the Ag-doped CoOOH

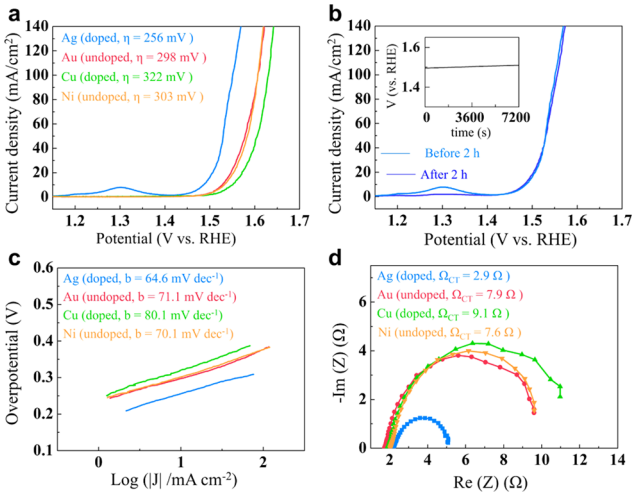

Figure 4. Electrochemical measurements of CoOOH on Ag, Au, Cu, and Ni. (a) OER polarization curves; (b) OER polarization curves before and after chronopotentiometric measurement of Ag-doped CoOOH; (c) Tafel plots; and (d) electrochemical impedance spectroscopy at 1.53 V (vs RHE). Inset (b) is a chronopotentiometry curve of Ag-doped CoOOH for 2 h at 10 mA/cm^2; all electrochemical measurements were conducted in O_2-saturated 1.0 M KOH.

electrocatalyst exhibited the highest OER performance with a 256 mV overpotential. In terms of durability, the Ag-doped CoOOH was maintained without any degradation for 2 h (see Figure 4b). Figure 4c shows the Tafel plot, which is a general indicator for the reaction kinetics of electrocatalysts.[43] The Ag-doped CoOOH shows the lowest Tafel slope of 64.6 mV/dec, indicating fast kinetics. More interestingly, Ag-doped CoOOH possesses an improved charge transfer property, Ω_{CT} = 2.9 Ω (Figure 4d), as recognized from the semicircle diameter of the EIS graph. The dramatically improved OER activity of the Ag-doped CoOOH could originate from the enhanced reaction kinetics and charge transfer between catalysts and the solvent provided by the homogeneously distributed Ag atoms. There exists a possibility that the enhanced OER performance of the Ag-doped CoOOH could be from the intrinsic electrical conductivity of the substrate. The conductivities of Ag, Au, Cu, and Ni at 20 °C are 6.30, 4.5, 5.89, and 1.39 (×10^7 S/m), respectively.[44] The CoOOH on Au substrate, having approximately three times higher conductivity than Ni substrate, showed almost the same overpotential and kinetics as CoOOH on the Ni substrate. Furthermore, we confirmed that CoOOH on Ag-electrodeposited Au substrate has an enhanced OER performance compared to CoOOH on Au (shown in Figure S13). These results imply that the enhanced OER property of Ag-doped CoOOH mainly originates from Ag doping effects and not from the intrinsic conductivity of the substrate.

3.5. Irreversible Redox Chemistry of Ag-Doped CoOOH. To understand the oxidation−reduction couples of the electrocatalysts, we conducted CV measurements of CoOOH on Ag, Au, Cu, and Ni, as shown in Figure 5a. In

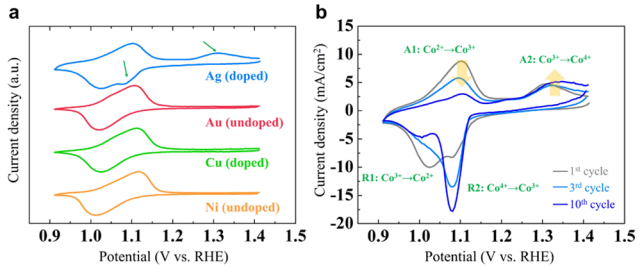

Figure 5. Irreversible redox electrochemistry of Ag-doped CoOOH. (a) Cyclic voltammetry (CV) measurements in the potential range of the phase transition for CoOOH on Ag, Au, Cu, and Ni (green arrows indicate oxidation−reduction peaks for further oxidation) and (b) multiple CV of Ag-doped CoOOH for 1st, 3rd, and 10th cycles.

the cases of Au, Cu, and Ni substrates, only one redox couple was observed, which corresponds to the phase transformation between Co^{2+} and Co^{3+}. On the other hand, the CoOOH on the Ag substrate shows new evolving peaks of the oxidation−reduction couple, as shown by the green arrows in Figure 5a. Bergmann et al. reported two distinct redox couples assigned to the phase transformations of $Co^{2+} \leftrightarrow Co^{3+}$ in the lower potential and $Co^{3+} \leftrightarrow Co^{4+}$ in the higher potential in the crystalline Co_3O_4 films.[15] Also, Liu et al. reported that the two anodic peaks of the electrodeposited $Co(OH)_2$ evolved in the CV prior to the OER, which was attributed to the oxidation of $Co^{2+} \leftrightarrow Co^{3+}$ and $Co^{3+} \leftrightarrow Co^{4+}$.[36] From these previous CV studies, the new evolving peaks in CoOOH on Ag can be related to the further oxidation of Co^{3+} to Co^{4+}. Moreover, the oxidation−reduction peaks for $Co^{2+} \leftrightarrow Co^{3+}$ in the low-potential region vanish after multiple CV scans, while the peaks for $Co^{3+} \leftrightarrow Co^{4+}$ grow (see Figure 5b). According to a previous study on the operando ambient-pressure XPS of Co-based oxide and hydroxide, further oxidation from CoOOH (Co^{3+}) to $CoO_{1+x}OH_{1-x}$ (Co^{4+}) was observed, and the Co^{4+} was suggested as an active state for robust OER.[14] Therefore, the irreversible reaction into the higher oxidation state in the case of Ag-doped CoOOH is a strong evidence of stabilizing the active phase by Ag dopants from the substrate.

The experimental observations can be summarized as follows: Ag atoms diffuse from the substrate into the catalyst during the activation; the oxidation state of Co changes due to Ag doping; the OER catalytic activity also increases through Ag doping in CoOOH. Further analyses of the phase stability and the improved catalytic activity were performed by DFT calculations to confirm experimental findings in the following part.

3.6. Theoretical Investigation of Ag Doping Effect. To better understand the experimental results, we performed DFT calculations. Figure S14a,b shows the computational surface Pourbaix diagrams of CoOOH ($10\bar{1}4$) and Ag-doped CoOOH ($10\bar{1}4$) slab models. At operating potentials of approximately 1.5 V, the stable CoOOH surface structure is covered with 1 ML of H_2O and 1 ML of OH, while the Ag-doped CoOOH surface has 1 ML of H_2O- and 4/6 ML of OH-covered surface.

DOI: 10.1021/acscatal.9b02249
ACS Catal. 2020, 10, 562−569

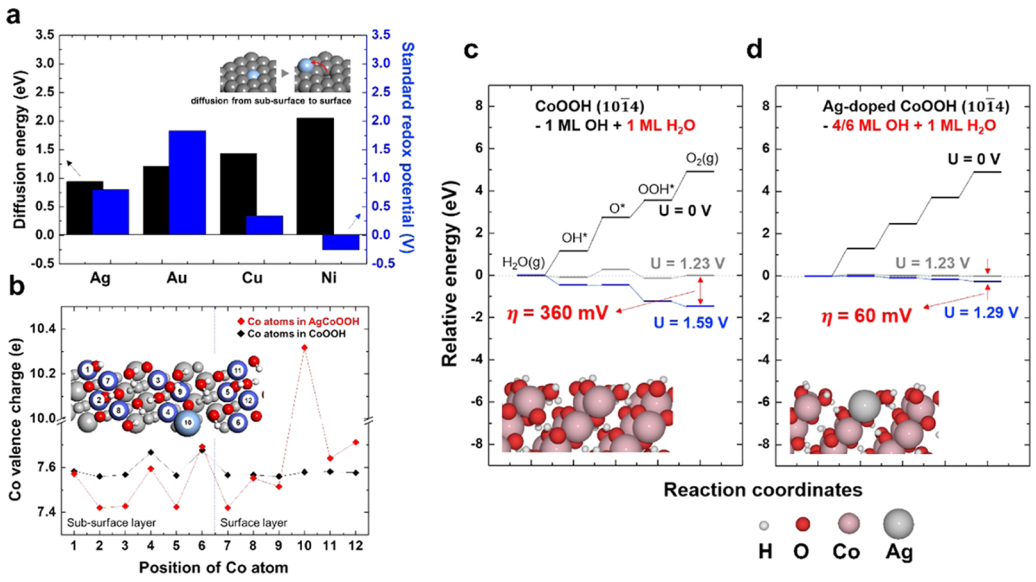

Figure 6. Theoretical investigations on Ag doping. (a) Diffusion energy barrier (black) and standard redox potential (blue) of each doping metal; (b) number of valence electrons transferred between CoOOH (black) and Ag-doped CoOOH (red): the blue star at position 10 represents the Ag element; and Gibbs free energy diagram with OER overpotential on (c) CoOOH (10$\bar{1}$4) and **d** (d) Ag-doped CoOOH (10$\bar{1}$4).

These calculated stable surface structures are shown in Figure 6c,d. From these results, we understand that Ag doping makes the OH− binding difficult on the near Ag sites, resulting in the lower OH− coverage at the Ag-doped CoOOH than the undoped CoOOH.

Among the various doping elements, only Ag and Cu can diffuse into CoOOH, based on Table S1. To understand these phenomena, we computed metal atom diffusion from the subsurface to the surface of CoOOH and calculated the standard reduction potentials of the given doping elements. Our expectation is that doping elements that easily oxidize and have low diffusion barriers should also diffuse into CoOOH.[45] Figure 6a shows that Ag, Cu, and Ni can be oxidized under 1.5 V—the same potential used to prepare the catalyst in this study. The energy barriers for the diffusion of each element, Ag, Au, Cu, and Ni, are 0.94, 1.21, 1.43, and 2.05 eV, respectively. Thus, Ag and Cu can diffuse into CoOOH but not Ni due to a high diffusion energy barrier as compared to the other doping elements.

To confirm phase stability of CoOOH by the oxidation state change of Co due to the Ag doping, we checked the valence charge of Co atoms in the subsurface and surface layer and determined the effect of Ag doping, as shown in Figure 6b. Most of the Co atoms in Ag-doped CoOOH are more oxidized with a smaller valence charge than those in undoped CoOOH (the red peak at the position 10 is due to the valence charge of the Ag atom). Ag, as a noble metal, has a low oxidation state, which forces the Co atoms into a high oxidation state to maintain the neutrality of the system. In other words, the enforced high oxidation state of Co atoms by Ag doping stabilizes the CoOOH phase.

The Gibbs free energy diagrams for the OER were calculated on the stable surface structures for each system to determine the overpotentials (see Figure 6c,d). Surprisingly, the Ag-doped CoOOH has a calculated overpotential of only 60 mV, which is significantly lower than the 360 mV overpotential for the undoped CoOOH. As shown in Figure S14b, the Ag-doped CoOOH is covered with 4/6 ML of OH* and 1 ML of H_2O, which is lower surface coverage than that of undoped CoOOH. We believe that the noble property of Ag makes OH* release from the CoOOH surface, and Ag atom became the new active site for the OER. We also checked the OER activity of Cu-doped CoOOH system to make sure Ag doping is the best among the experimentally controlled systems. As shown in Figure S15, we evaluated the surface Pourbaix diagram of Cu-doped CoOOH to identify the exact surface condition when OER actually happens and found that Cu-doped CoOOH had a very high overpotential (1300 mV), even higher than that of the undoped CoOOH system. However, the actual activity will not be much different from the undoped CoOOH because of a low doping concentration, and a majority of the surface would be covered with the undoped CoOOH. There will be an influence by the Cu doping, but the effect would not be critical.

4. CONCLUSIONS

A highly active Ag-doped CoOOH nanosheet arrays were fabricated using two-step electrodeposition of $Co(OH)_2$, followed by an activation process. The activation process not only further oxidized Co^{2+} to Co^{3+} but also led to Ag^+ diffusion. The homogenous distribution of Ag cations was confirmed with several experimental techniques including HAADF-STEM, EDS mapping, and TOF-SIMS. Moreover, APT analysis showed the absence of segregation and the homogeneously distributed Ag dopants near the surface. The Ag-doped CoOOH exhibited a 256 mV overpotential for the OER, a 64.6 mV/dec Tafel slope, and 2.9 Ω of charge transfer resistance. This OER performance was maintained for over 2 h. Compared to Co-based OER electrocatalysts in recent reports (Table S2), the Ag-doped CoOOH electrocatalyst is shown, in this work, to have a remarkably high performance. DFT calculations showed a theoretical overpotential of only 60 mV as a result of exposed Ag atoms releasing OH− adsorbates to provide new active sites for OER. The dopant Ag atoms were found to stabilize the active phase (CoOOH, Co^{3+}) for the OER, supported by our theoretical Bader charge analysis. This facile doping strategy can open a new pathway to highly active transition metal-doped systems without surface segregation,

DOI: 10.1021/acscatal.9b02249
ACS Catal. 2020, 10, 562−569

which could have a significant impact on the development of novel electrocatalysts.

■ ASSOCIATED CONTENT

Supporting Information

The Supporting Information is available free of charge at https://pubs.acs.org/doi/10.1021/acscatal.9b02249.

DFT calculations; EDS cross-sectional maps; ICP-OES compositions; EDS compositions; additional SEM and TEM images; SIMS data; XRD and XPS analyses; surface free energy diagrams; Gibbs free energy diagram (PDF)

■ AUTHOR INFORMATION

Corresponding Authors

*E-mail: henkelman@utexas.edu (G.H.).
*E-mail: hmlee@kaist.ac.kr (H.M.L.).

ORCID

Kihyun Shin: 0000-0002-1748-8773
Pyuck-Pa Choi: 0000-0001-9920-0755
Graeme Henkelman: 0000-0002-0336-7153
Hyuck Mo Lee: 0000-0003-4556-6692

Author Contributions

C.L., K.S., and C.J. contributed equally to this work. C.L. and H.M.L. conceived an idea and led the overall project. C.L. carried out the electrochemical synthesis and analyses. K.S. and G.H. performed DFT calculations. C.J. and P.-P.C. carried out APT and HAADF-STEM analyses. All authors discussed and commented on the manuscript.

Notes

The authors declare no competing financial interest.

■ ACKNOWLEDGMENTS

This research was supported by the National Research Foundation of Korea (NRF) grant funded by the Korean Government (MSIT) (Nos. NRF-2015R1A5A1037627 and NRF-2017R1E1A1A03071049). Computational work at UT Austin was supported by the Welch Foundation (F-1841) and the Texas Advanced Computing Center.

■ REFERENCES

(1) Buttler, A.; Spliethoff, H. Current Status of Water Electrolysis for Energy Storage, Grid Balancing and Sector Coupling via Power-to-Gas and Power-to-Liquids: A Review. *Renewable Sustainable Energy Rev.* **2018**, *82*, 2440−2454.

(2) Nikolic, V. M.; Tasic, G. S.; Maksic, A. D.; Saponjic, D. P.; Miulovic, S. M.; Kaninski, M. P. M. Raising Efficiency of Hydrogen Generation from Alkaline Water Electrolysis - Energy Saving. *Int. J. Hydrogen Energy* **2010**, *35*, 12369−12373.

(3) Cook, T. R.; Dogutan, D. K.; Reece, S. Y.; Surendranath, Y.; Teets, T. S.; Nocera, D. G. Solar Energy Supply and Storage for the Legacy and Non legacy Worlds. *Chem. Rev.* **2010**, *110*, 6474−6502.

(4) Hong, W. T.; Risch, M.; Stoerzinger, K. A.; Grimaud, A.; Suntivich, J.; Shao-Horn, Y. Toward the Rational Design of Non-Precious Transition Metal Oxides for Oxygen Electrocatalysis. *Energy Environ. Sci.* **2015**, *8*, 1404−1427.

(5) McCrory, C. C. L.; Jung, S. H.; Peters, J. C.; Jaramillo, T. F. Benchmarking Heterogeneous Electrocatalysts for the Oxygen Evolution Reaction. *J. Am. Chem. Soc.* **2013**, *135*, 16977−16987.

(6) Fan, K.; Chen, H.; Ji, Y. F.; Huang, H.; Claesson, P. M.; Daniel, Q.; Philippe, B.; Rensmo, H.; Li, F.; Luo, Y.; Sun, L. Nickel-Vanadium Monolayer Double Hydroxide for Efficient Electrochemical Water Oxidation. *Nat. Commun.* **2016**, *7*, No. 11981.

(7) Subbaraman, R.; Tripkovic, D.; Chang, K.-C.; Strmcnik, D.; Paulikas, A. P.; Hirunsit, P.; Chan, M.; Greeley, J.; Stamenkovic, V.; Markovic, N. M. Trends in Activity for the Water Electrolyser Reactions on 3d M(Ni,Co,Fe,Mn) Hydr(oxy)oxide Catalysts. *Nat. Mater.* **2012**, *11*, 550−557.

(8) Chen, W.; Wang, H.; Li, Y.; Liu, Y.; Sun, J.; Lee, S.; Lee, J.-S.; Cui, Y. In Situ Electrochemical Oxidation Tuning of Transition Metal Disulfides to Oxides for Enhanced Water Oxidation. *ACS Cent. Sci.* **2015**, *1*, 244−251.

(9) Li, Q.; Wang, X.; Tang, K.; Wang, M.; Wang, C.; Yan, C. Electronic Modulation of Electrocatalytically Active Center of Cu_7S_4 Nanodisks by Cobalt-Doping for Highly Efficient Oxygen Evolution Reaction. *ACS Nano* **2017**, *11*, 12230−12239.

(10) Liang, Y.; Li, Y.; Wang, H.; Zhou, J.; Wang, J.; Regier, T.; Dai, H. Co_3O_4 Nanocrystals on Graphene as a Synergistic Catalyst for Oxygen Reduction Reaction. *Nat. Mater.* **2011**, *10*, 780−786.

(11) Grimaud, A.; Diaz-Morales, O.; Han, B. H.; Hong, W. T.; Lee, Y.-L.; Giordano, L.; Stoerzinger, K. A.; Koper, M. T. M.; Shao-Horn, Y. Activating Lattice Oxygen Redox Reactions in Metal Oxides to Catalyse Oxygen Evolution. *Nat. Chem.* **2017**, *9*, 457−465.

(12) Cho, S.-H.; Yoon, K. R.; Shin, K.; Jung, J.-W.; Kim, C.; Cheong, J. Y.; Youn, D.-Y.; Song, S. W.; Henkelman, G.; Kim, I.-D. Synergistic Coupling of Metallic Cobalt Nitride Nanofibers and IrOx Nanoparticle Catalysts for Stable Oxygen Evolution. *Chem. Mater.* **2018**, *30*, 5941−5950.

(13) Kim, J.-H.; Shin, K.; Kawashima, K.; Youn, D. H.; Lin, J.; Hong, T. E.; Liu, Y.; Wygant, B. R.; Wang, J.; Henkelman, G.; Mullins, C. B. Enhanced Activity Promoted by CeO_x on a CoO_x Electrocatalyst for the Oxygen Evolution Reaction. *ACS Catal.* **2018**, *8*, 4257−4265.

(14) Favaro, M.; Yang, J. H.; Nappini, S.; Magnano, E.; Toma, F. M.; Crumlin, E. J.; Yano, J.; Sharp, I. D. Understanding the Oxygen Evolution Reaction Mechanism on CoO_x using Operando Ambient-Pressure X-ray Photoelectron Spectroscopy. *J. Am. Chem. Soc.* **2017**, *139*, 8960−8970.

(15) Bergmann, A.; Martinez-Moreno, E.; Teschner, D.; Chernev, P.; Gliech, M.; de Araujo, J. F.; Reier, T.; Dau, H.; Strasser, P. Reversible Amorphization and the Catalytically Active State of Crystalline Co_3O_4 during Oxygen Evolution. *Nat. Commun.* **2015**, *6*, No. 8625.

(16) Zhang, R.; Zhang, Y.-C.; Pan, L.; Shen, G.-Q.; Mahmood, N.; Ma, Y.-H.; Shi, Y.; Jia, W.; Wang, L.; Zhang, X.; Xu, W.; Zou, J.-J. Engineering Cobalt Defects in Cobalt Oxide for Highly Efficient Electrocatalytic Oxygen Evolution. *ACS Catal.* **2018**, *8*, 3803−3811.

(17) Sultana, U. K.; Riches, J. D.; O'Mullane, A. P. Gold Doping in a Layered Co-Ni Hydroxide System via Galvanic Replacement for Overall Electrochemical Water Splitting. *Adv. Funct. Mater.* **2018**, *28*, No. 1804361.

(18) Zhao, X.; Zhang, H.; Yan, Y.; Cao, J.; Li, X.; Zhou, S.; Peng, Z.; Zeng, J. Engineering the Electrical Conductivity of Lamellar Silver-Doped Cobalt(II) Selenide Nanobelts for Enhanced Oxygen Evolution. *Angew. Chem., Int. Ed.* **2017**, *56*, 328−332.

(19) Suksomboon, M.; Khuntilo, J.; Kalasina, S.; Suktha, P.; Limtrakul, J.; Sawangphruk, M. High-Performance Energy Storage of Ag-Doped $Co(OH)_2$-Coated Graphene Paper: In Situ Electrochemical X-ray absorption Spectroscopy. *Electrochim. Acta* **2017**, *252*, 91−100.

(20) Yan, K.-L.; Chi, J.-Q.; Xie, J.-Y.; Dong, B.; Liu, Z.-Z.; Gao, W.-K.; Lin, J.-H.; Chai, Y.-M.; Liu, C.-G. Mesoporous Ag-Doped Co_3O_4 Nanowire Arrays Supported on FTO as Efficient Electrocatalysts for Oxygen Evolution Reaction in Acidic Media. *Renewable Energy* **2018**, *119*, 54−61.

(21) Zeng, Z.; Sun, P.; Zhu, J.; Zhu, X. Ag-Doped Manganese Oxide Prepared by Electrochemical Deposition on Carbon Fiber for Supercapacitors. *RSC Adv.* **2015**, *5*, 17550−17558.

(22) Huang, X.; Xie, M.; Chen, Y.; Zong, Q.; Liu, Z.; Jin, Y. Copper-Silver Oxide Nanowires Grown on an Alloy Electrode as an Efficient Electrocatalyst for Water Oxidation. *RSC Adv.* **2015**, *5*, 26150−26156.

(23) Maier, J. Nanoionics: Ion Transport and Electrochemical Storage in Confined Systems. *Nat. Mater.* **2005**, *4*, 805−815.

DOI: 10.1021/acscatal.9b02249
ACS Catal. 2020, 10, 562−569

(24) Waser, R.; Aono, M. Nanoionics-Based Resistive Switching Memories. *Nat. Mater.* **2007**, *6*, 833−840.
(25) Wang, X.; Zhuang, L.; He, T.; Jia, Y.; Zhang, L.; Yen, X.; Gao, M.; Du, A.; Zhu, Z.; Yao, X.; Yu, S.-H. Grafting Cobalt Diselenide on Defective Graphene for Enhanced Oxygen Evolution Reaction. *iScience* **2018**, *7*, 145−153.
(26) Prosa, T. J.; Lawrence, D.; Olson, D.; Larson, D. J.; Marquis, E. A. Backside Lift-Out Specimen Preparation: Reversing the Analysis Direction in Atom Probe Tomography. *Microsc. Microanal.* **2009**, *15*, 298−299.
(27) Perdew, J. P.; Burke, K.; Ernzerhof, M. Generalized Gradient Approximation Made Simple. *Phys. Rev. Lett.* **1996**, *77*, No. 3865.
(28) Bajdich, M.; Garcia-Mota, M.; Vojvodic, A.; Norskov, J. K.; Bell, A. T. Theoretical Investigation of the Activity of Cobalt Oxides for the Electrochemical Oxidation of Water. *J. Am. Chem. Soc.* **2013**, *135*, 13521−13530.
(29) García-Mota, M.; Bajdich, M.; Viswanathan, V.; Vojvodic, A.; Bell, A. T.; Norskov, J. K. Importance of Correlation in Determining Electrocatalytic Oxygen Evolution Activity on Cobalt Oxides. *J. Phys. Chem. C* **2012**, *116*, 21077−21082.
(30) Hansen, H. A.; Rossmeisl, J.; Norskov, J. K. Surface Pourbaix Diagrams and Oxygen Reduction Activity of Pt, Ag and Ni(111) Surfaces Studied by DFT. *Phys. Chem. Chem. Phys.* **2008**, *10*, 3722−3730.
(31) Ping, Y.; Nielsen, R. J.; Goddard, W. A. The Reaction Mechanism with Free Energy Barriers at Constant Potentials for the Oxygen Evolution Reaction at the IrO_2 (110) Surface. *J. Am. Chem. Soc.* **2017**, *139*, 149−155.
(32) Meng, S.; Wang, E. G.; Gao, S. Water Adsorption on Metal Surfaces: A General Picture from Density Functional Theory Studies. *Phys. Rev. B* **2004**, *69*, No. 195404.
(33) Man, I. C.; Su, H.-Y.; Calle-Vallejo, F.; Hansen, H. A.; Martinez, J. I.; Inoglu, N. G.; Kitchin, J.; Jaramillo, T. F.; Norskov, J. K.; Rossmeisl, J. Universality in Oxygen Evolution Electrocatalysis on Oxide Surfaces. *ChemCatChem* **2011**, *3*, 1159−1165.
(34) Patil, U. M.; Nam, M. S.; Sohn, J. S.; Kulkarni, S. B.; Shin, R.; Kang, S.; Lee, S.; Kim, J. H.; Jun, S. C. Controlled Electrochemical Growth of $Co(OH)_2$ Flakes on 3D Multilayered Graphene Foam for High Performance Supercapacitors. *J. Mater. Chem. A* **2014**, *2*, 19075−19083.
(35) Nguyen, T.; Boudard, M.; Carmezim, M. J.; Montemor, M. F. Layered $Ni(OH)_2$-$Co(OH)_2$ Films Prepared by Electrodeposition as Charge Storage Electrodes for Hybrid Supercapacitors. *Sci. Rep.* **2017**, *7*, No. 39980.
(36) Liu, Y.-C.; Koza, J. A.; Switzer, J. A. Conversion of Electrodeposited $Co(OH)_2$ to CoOOH and Co_3O_4, and Comparison of Their Catalytic Activity for the Oxygen Evolution Reaction. *Electrochim. Acta* **2014**, *140*, 359−365.
(37) Pralong, V.; Delahaye-Vidal, A.; Beaudoin, B.; Gerand, B.; Tarascon, J. M. Oxidation Mechanism of Cobalt Hydroxide to Cobalt Oxyhydroxide. *J. Mater. Chem.* **1999**, *9*, 955−960.
(38) Yang, J.; Liu, H.; Martens, W. N.; Frost, R. L. Synthesis and Characterization of Cobalt Hydroxide, Cobalt Oxyhydroxide, and Cobalt Oxide Nanodiscs. *J. Phys. Chem. C* **2010**, *114*, 111−119.
(39) Lin, T.-C.; Seshadri, G.; Kelber, J. A. A Consistent Method for Quantitative XPS Peak Analysis of Thin Oxide Films on Clean Polycrystalline Iron Surfaces. *Appl. Surf. Sci.* **1997**, *119*, 83−92.
(40) Zhuang, L.; Ge, L.; Yang, Y.; Li, M.; Jia, Y.; Yao, X.; Zhu, Z. Ultrathin Iron-Cobalt Oxide Nanosheets with Abundant Oxygen Vacancies for the Oxygen Evolution Reaction. *Adv. Mater.* **2017**, *29*, No. 1606793.
(41) Zhang, B.; Zhang, J.; Tan, X.; Tan, D.; Shi, J.; Zhang, F.; Liu, L.; Su, Z.; Han, B.; Zheng, L.; Zhang, J. One-Step Synthesis of Ultrathin Alpha-$Co(OH)_2$ Nanomeshes and Their High Electrocatalytic Activity toward the Oxygen Evolution Reaction. *Chem. Commun.* **2018**, *54*, 4045−4048.
(42) McCrory, C. C. L.; Jung, S.; Ferrer, I. M.; Chatman, S. M.; Peters, J. C.; Jaramillo, T. F. Benchmarking Hydrogen Evolving Reaction and Oxygen Evolving Reaction Electrocatalysts for Solar Water Splitting Devices. *J. Am. Chem. Soc.* **2015**, *137*, 4347−4357.
(43) Fang, Y.-H.; Liu, Z.-P. Tafel Kinetics of Electrocatalytic Reactions: From Experiment to First-Principles. *ACS Catal.* **2014**, *4*, 4364−4376.
(44) Khanna, S. N.; Jain, A. Electrical-Resistivity of Noble and Transition-Metals Using Animalus Model Potential. *J. Phys. Chem. Solids* **1977**, *38*, 447−450.
(45) Wu, H.; Mayeshiba, T.; Morgan, D. High-Throughput ab-Initio Dilute Solute Diffusion Database. *Sci. Data* **2016**, *3*, No. 160054.

DOI: 10.1021/acscatal.9b02249
ACS Catal. 2020, 10, 562−569